Accepted Article Preview: Published ahead of advance online publication

A Non-volatile Switchable Infrared Stealth Metafilm with GST

Cong Quan, Song Gu, Tingzhao Fu, Ping Liu, Wei Xu, Chucai Guo, Zhihong Zhu, and Jianfa Zhang

A Non-volatile Switchable Infrared Stealth Metafilm with GST

Cong Quan[1,2], **Song Gu**[1,2], **Tingzhao Fu**[1,2], **Ping Liu**[1,2], **Wei Xu**[1,2], **Chucai Guo**[1,2], **Zhihong Zhu**[1,2, *], **and Jianfa Zhang**[1,2, *]

[1] College of Advanced Interdisciplinary Studies, National University of Defense Technology, Changsha 410073, China.

[2] Hunan Provincial Key Laboratory of Novel Nano-Optoelectronic Information Materials and Devices, National University of Defense Technology, Changsha 410073, China.

*zzhwcx@163.com

*jfzhang85@nudt.edu.cn

Abstract

In this paper, we experimentally demonstrate a non-volatile switchable infrared stealth metafilm based on high temperature resistant metal Molybdenum (Mo) and phase change material $Ge_2Sb_2Te_5$(GST). By controlling the phase state of GST, the switch between the infrared stealth and the non-stealth states can be realized. Specifically, when the GST is in the amorphous state, the emissivity of the film in the 3-5 μm and 8-14 μm atmospheric window band is suppressed and can realize infrared stealth, together with a high absorption peak of 94% at 6.08 μm, which enables radiative heat dissipation; While for the crystalline state of the GST, the average emissivity is more than 0.7 in the band of 8-14 μm, and the infrared stealth function cannot be realized. When the background temperature is 100°C, the temperature difference between the two samples reaches as high as 28°C under an infrared thermal imager. Therefore, our proposed metafilm can flexibly regulate the infrared thermal radiation of the target so as to realize the switch between the infrared stealth and non-stealth state. We have fabricated the metafilm on both hard and flexible substrates. Our work holds profound significance for the study of dynamic thermal

radiation control and it is set to pave the way for the practical implementation of intelligent infrared stealth technology.

Introduction

Infrared stealth technology is defined by the reduction of an object's infrared emissions or the alteration of its infrared signature, thereby reducing the possibility of being detected by infrared detection systems[1-6]. With the rapid development of nanophotonics, infrared stealth technology has made significant breakthroughs in recent years[7-9]. At the beginning, the infrared stealth was generally realized by reducing the infrared radiation and using low-emissivity coatings. According to the Stephen-Boltzmann's law[10], the infrared radiation of the target is proportional to the emissivity and the fourth power of the absolute temperature. Consequently, by reducing emissivity to achieve infrared stealth, the heat will continue to accumulate, together with the rise in temperature, which ultimately compromises the stealth capabilities. To solve this problem, more and more research focuses on infrared stealth technology that can achieve spectrally selective control of the infrared radiation characteristics[11-16]. By reducing the infrared radiation in the atmospheric window band of 3-5 μm and 8-14 μm that the current infrared detection system works on, the infrared stealth can be realized[17-21]. At the same time, the radiation in the non-atmospheric window band of 5-8 μm is maintained or even increased to realize radiative heat dissipation[22-26].

To date, spectrally selective infrared stealth technology has achieved great sucess[27-29]. One of the most representative methods is the structural design of metamaterials[30-36]. Metamaterials are artificial materials with novel physical properties that traditional materials cannot achieve, which are generally realized by the design and manipulation of micro- or nano-structures in the sub-wavelength scale[37-46]. According to Kirchhoff's law of thermal radiation[47], the spectral emissivity and absorptivity of an object in thermal equilibrium are equal. Therefore, the regulation of absorptivity of the object is equivalent

to that of the emissivity. By constructing metamaterials with different structures, the optical absorptivity can be controlled, so that the spectrally selective infrared stealth function can be well realized. However, these methods are only aimed at the stealth in specific background environment. As the background environment is not static in practical applications, this stealth state will be broken once the external environment changes. Therefore, tunable infrared stealth technology has become the center of many recent researches.

Generally speaking, one of the commonly used tuning strategies is combing stealth structures with active materials, which can change the optical properties through external stimulation, so as to regulate the infrared radiation characteristics of the entire structure[30, 32]. However, the response of most active materials to external stimuli is volatile, i.e. the external stimulus conditions need to be maintained to stabilize its optical properties in a certain state. To realize non-volatile switch, phase change materials are widely used [48-52]. Among them, one of the most common materials is $Ge_2Sb_2Te_5$(GST), which has two different states: in the amorphous state, the internal atomic distribution is very chaotic, and the imaginary part of the relative permittivity in the infrared band is almost 0; When it turns to the crystal state, the relative permittivity will be significantly increased, and the absorption is higher than that in the amorphous state[53-58].

Therefore, in this paper, by using GST with the characteristics of phase change material, and the high temperature resistant metal Mo (for high temperature may be generated in the annealing process), we propose a switchable infrared stealth bilayer metafilm. When the GST is in the amorphous state, the absorptivity of the structure in the atmospheric window band is relatively low, together with the high absorptivity in the non-atmospheric window band, which can realize the infrared stealth while taking into account the radiation heat dissipation ability in the non-atmospheric window; When the GST switches to the crystal state, the absorptivity of the film in the atmospheric window band prominently increases, and the stealth function cannot be realized. By adjusting the GST in different states, the target can switch between the infrared stealth and the non-stealth states, while the infrared radiation characteristics can be flexibly controlled to adapt to the complex and changeable external environment.

Structural design

Figure 1(a) shows the detection mechanism of the infrared detectors. The infrared radiation emitted by the target is transmitted through the atmosphere and captured by the infrared detector. Figure 1(b) depicts the schematic diagram of the designed tunable infrared stealth bilayer metafilm based on the bottom metal Mo layer and the top phase change material GST layer, together with the schematic diagram of the transition mechanism of GST between different states. The structure is optimized and the thicknesses of the two layers are $H_1 = 100\ nm$ and $H_2 = 360\ nm$, respectively.
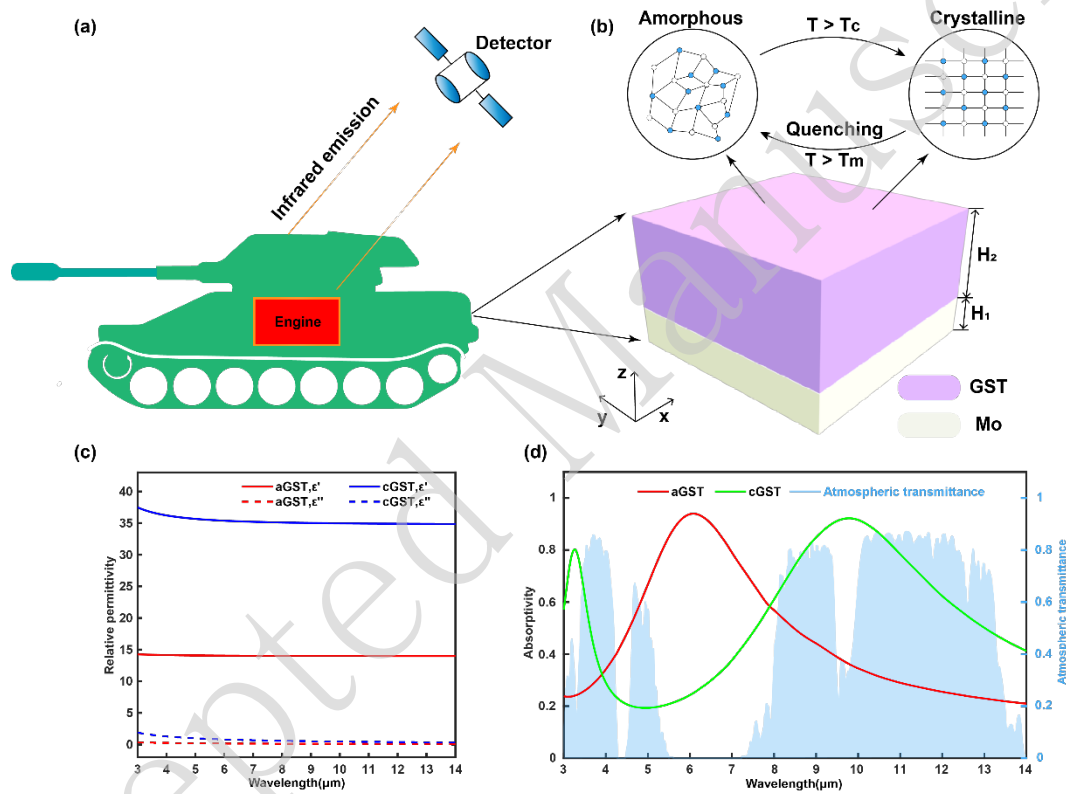

Figure 1. The structure diagram and the absorption spectra obtained by simulation under normal incidence. (a) The detection mechanism of the infrared detectors. The infrared radiation of the target is transmitted through the atmosphere and captured by the infrared detector. **(b)** Schematic diagram of the bilayer metafilm and the transition mechanism of GST between different states. When the temperature exceeds the crystallization temperature T_c, the GST will gradually change from amorphous state to the crystalline state, and once the temperature exceeds the melting temperature T_m, after rapid annealing, the GST can change back to the amorphous state. **(c)** The relative permittivity of GST at different states in infrared band measured by the spectroscopic ellipsometer. **(d)** The absorption spectra of the metafilm with two phase states for normally incident light and the atmospheric transmittance spectrum.

The metafilm consists of a simple bilayer structure and the absorption spectra can be calculated by numerical simulations as well as analytical methods (Supplement Figure S1).

Here, in order to study the field distributions of structure, we conduct numerical simulations by using the commercial solver of COMSOL Multiphysics. As the structure extends indefinitely in both x and y directions, we take the cross section in $x - z$ direction in the simulation and set periodic boundary conditions on each side with the port conditions on the upper and lower boundaries. Firstly, we consider the case of normal incidence. Due to the high symmetry of the structure, it is polarization-independent for the normal incident light and the spectra are the same for the two polarization states, so here we only consider the incident light at TM mode (magnetic field vector is perpendicular to the incident plane). The relative permittivity of GST and Mo in infrared band is measured by a spectroscopic ellipsometer as shown in Figure 1(c) and Supplement Figure S2(a). The relative permittivity significantly increases when it turns to the crystal state. As the substrate material Mo is optically thick, the transmission of the whole structure is close to zero. Thus, the near-unity absorption can be implemented if the reflection coefficient decreases to zero by selecting the appropriate thickness of the layers to match the impedance of the film with the air. The simulated absorption spectra of the film along the atmospheric transmittance spectrum are shown in Figure 1(d). In order to better compare the infrared radiation characteristics of different bands, we calculate the average emissivity in each band, as shown in the formula (1-2). Among them, $M_b(T, \lambda)$ is the spectral radiance of the blackbody calculated from Planck's blackbody radiation law[59], h, c, k, T is Planck's constant, the velocity of light in vacuum, the Boltzmann's constant and temperature; $\varepsilon_{f, \lambda_1 \sim \lambda_2}$ is the average emissivity of the film in the wavelength band $\lambda_1 \sim \lambda_2$; $\varepsilon_f(T, \lambda)$ is the spectral emissivity. When the GST is in the amorphous state, the infrared radiation of the film in the 3-5 μm and 8-14 μm atmospheric window band is relatively low, which can realize infrared stealth. In the non-atmospheric window band, the infrared radiation significantly improves, and a high absorption peak at 6.08 μm is observed with an absorptivity of 94%. At the same time, the average emissivity is over 0.7, which demonstrates great radiative heat dissipation ability. While for the crystal state of the GST, the average emissivity in the band of 8-14 μm significantly increases to over 0.7, and the structure turns to the non-stealth state. Therefore, by changing the GST into different states, the switch between the infrared stealth and the non-stealth state of the target can be achieved.

$$M_b(T, \lambda) = \frac{2\pi h c^2}{\lambda^5} \times \frac{1}{e^{hc/\lambda kT} - 1} \tag{1}$$

$$\varepsilon_{f,\lambda_1 \sim \lambda_2} = \frac{\int_{\lambda_1}^{\lambda_2} \varepsilon_f(T,\lambda) \times M_b(T,\lambda) d\lambda}{\int_{\lambda_1}^{\lambda_2} M_b(T,\lambda) d\lambda} \tag{2}$$

To interpret the absorption mechanism of the metafilm, we plot the electric field distribution and power loss diagram at the absorption peaks in Figure 1(d), which corresponds to three resonance wavelengths of $\lambda_1 = 6.08 \, \mu m$, $\lambda_2 = 3.26 \, \mu m$ and $\lambda_3 = 9.78 \, \mu m$ for the different states of GST. As shown in Figure 2, we can find that the electric field is mainly concentrated in the upper GST layer with its maximum near the top surface. From the relative permittivity curve of the material (Supplement Figure S2), we can find that compared with Mo, the imaginary part of the relative permittivity of the GST is much lower, whether in the amorphous state or in the crystalline state, so the absorption of the structure is mainly concentrated in the lower Mo layer, which can also be visually found from the power loss diagram. Moreover, due to the significant increase in the real part of the relative permittivity after the transformation from the amorphous state to the crystalline state of GST, the absorption spectrum of the structure has been redshifted, and the wavelength of the resonance absorption peak has moved from 6.08 μm to 9.78 μm. Besides, there is also an additional absorption peak at 3.26 μm that is previously located in the near infrared band (not shown here). Meanwhile, from Figure 2(c) and (e), it can be found that due to the stronger electric field in the Mo layer at 9.78 μm, the absorption of the structure is also improved compared with that at 3.26 μm, which is consistent with the results shown in the absorption spectra in Figure 1(d).
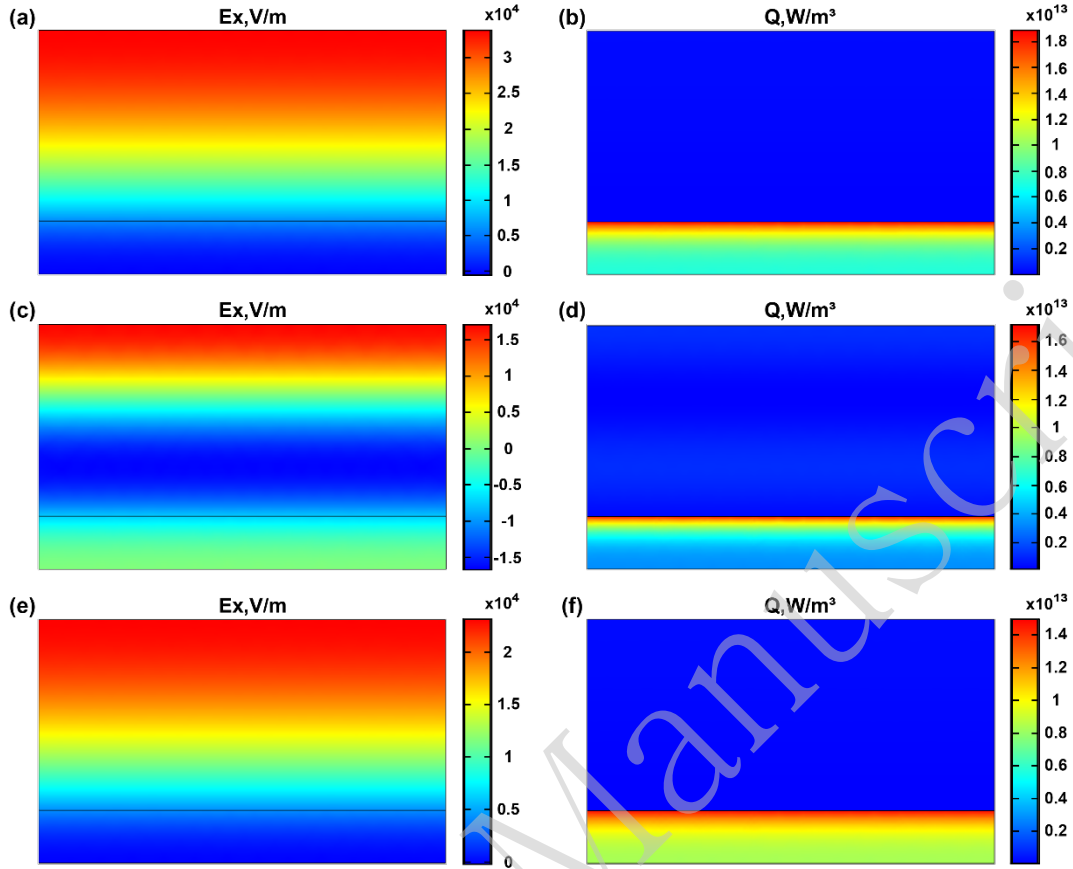
Figure 2. The absorption mechanism of the metafilm. (a) The electric field distribution and (**b**) power loss diagram at the resonance absorption peak of 6.08 μm when GST is in the amorphous state. (**c**) The electric field distribution and power loss diagram (**d**) at the resonance absorption peak of 3.26 μm when GST is in the crystalline state. (**e**) The electric field distribution and (**f**) power loss diagram at the resonance absorption peak of 9.78 μm when GST is in the crystalline state.

Then, the angular dependence of optical absorption with TE and TM polarizations for different phase states of GST is studied, as shown in Figure 3. It can be seen that in the investigated spectral range, the absorptivity barely changes with the increase of the incidence angle within 40 degrees, which can maintain more than 90%. The simulated results demonstrate that the proposed metafilm maintains good performance of infrared stealth with polarization-independent and wide-angle responses.
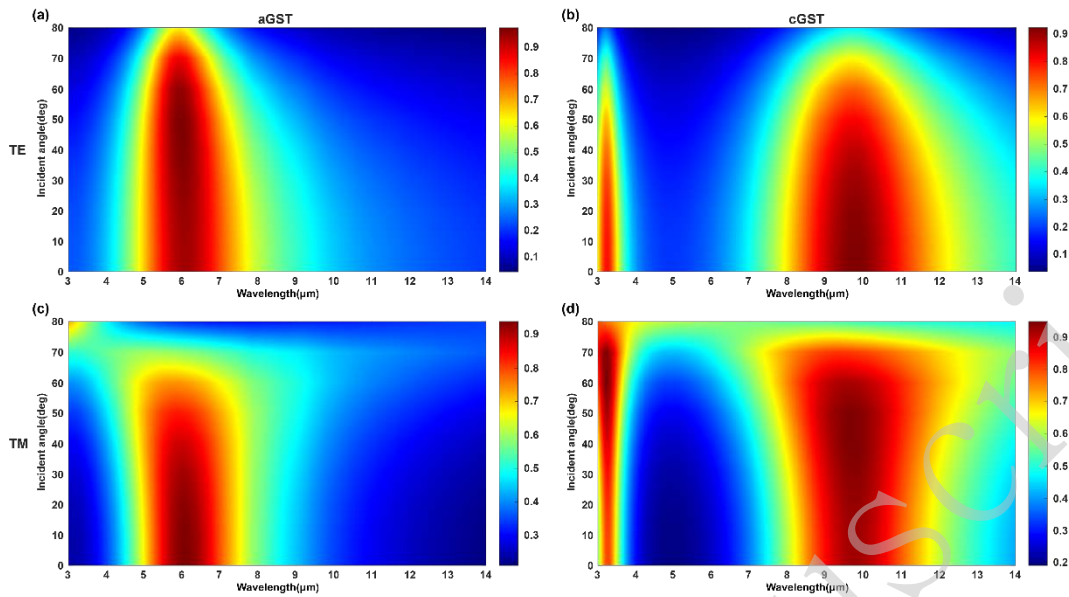
Figure 3. The influence of the polarization state and incident angle to the absorption of the metafilm. Calculated absorptivity of different incident angles at **(a)** TE and **(c)** TM mode oblique incidences when GST is in the amorphous state. Calculated absorptivity of different incident angles at **(b)** TE and **(d)** TM mode oblique incidences when GST is in the crystalline state.

Experimental demonstration

We further experimentally demonstrate the excellent switchable characteristics of the infrared stealth metafilm. Following the optimized structural parameters in simulations, the corresponding GST-Mo bilayer samples are prepared. Initially, a Mo film with a thickness of $100\ nm$ is deposited on a meticulously cleaned silicon substrate with a $285\ nm$ oxide layer by high vacuum magnetron sputtering under room temperature. Subsequently a $360\ nm$ GST layer is deposited on top of it. The deposited GST in the prepared samples is at a phase state that close to the amorphous state, and by heating the sample on a heating stage at 200°C (slightly above the crystallization temperature) for 10 minutes, we successfully complete the phase transition to the crystal stage. The samples are shown in Figure 4(a) for the different states of GST, and the size of them are roughly $1\ cm \times 1\ cm$. Additionally, due to the good ductility of the two materials we used, it can be fabricated on flexible substrates like PET, as shown in Figure 4(b). Since there is a certain absorption in the visible band (Supplement Figure S4), these samples appear dark. The cross-section pictures of the prepared bilayer film at the two stages of GST under the scanning electron microscope (SEM) are shown in Figures 4(c) and 4(d). It can be seen that after phase transition of GST from amorphous state to crystalline state, its internal

structure becomes more ordered, for a large number of microcrystalline structures appear. The infrared absorption spectra of the samples at different phase conditions are obtained by a Fourier transform infrared spectrometer (FTIR) as shown in Figure 5(a). Consistent with simulation results, it is evident that when GST switches from amorphous state to crystalline state, there is significant alteration in the infrared absorption/emission. Specifically, when the GST is in the amorphous state, the film can realize the infrared stealth function, while capable of good radiative heat dissipation capability. But once the GST is transformed into a crystalline state, due to the significant increase in the relative permittivity of the GST, the absorption spectrum of the entire structure is significantly redshifted, resulting in the huge increase of the infrared radiation of the structure in the 8-14 μm atmospheric window, so that the stealth function cannot be realized. Therefore, by switching between different states of GST, the film can be switched between the infrared stealth and the non-stealth states.

However, upon comparing the absorption spectra between simulation and experiment, we observe a slight deviation in the experimental measurements when the GST transitions to its crystalline state. This is evident from an apparent blue shift in the absorption spectra (Supplement Figure S5(a)). Further investigations reveal a reduction in the thickness of the upper GST layer of the bilayer films during the transition from amorphous to crystalline phase, which is only about 330 nm compared with the 360 nm before. Therefore, we recalibrate the thickness of GST after the phase transition in the simulation and obtain a new absorption spectrum (Supplement Figure S5(b)). Notably, following these adjustments, it becomes evident that our sample's measured infrared spectra agree well with our simulation results. When the GST is in the amorphous state, the average emissivity of the film in the 3-5 μm and 8-14 μm atmospheric window band are 0.31 and 0.24, respectively, enabling infrared stealth. However, within non-atmospheric window band of 5-8 μm, it demonstrates an average emissivity of 0.67 which facilitates radiative heat dissipation. When the state of GST changes to crystalline, the average emissivity of the structure in 8-14 μm exceeds 0.67, which is highly consistent with the results obtained by our simulations.
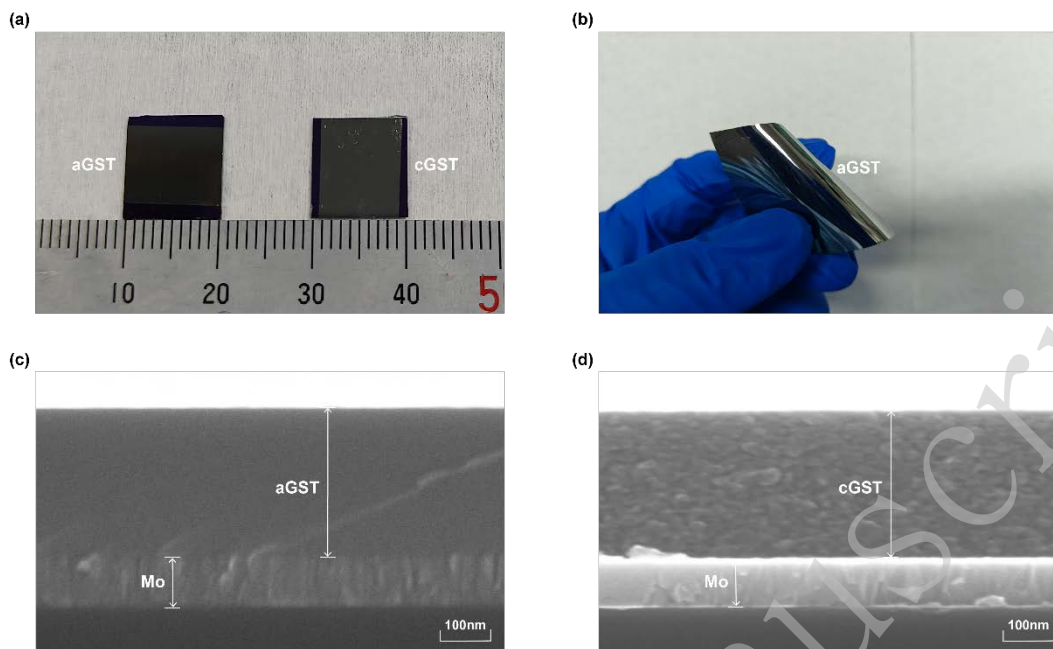
Figure 4. Fabricated metafilms based on the phase change material GST. (a) The images of prepared bilayer film on the silicon substrate at the different stages of GST. (**b**) The image of prepared bilayer film on the flexible substrate PET. The cross-section images of the prepared bilayer metafilm under scanning electron microscope (SEM) when GST is in the (**c**) amorphous (**d**) crystalline states.

Then, we study the infrared radiation properties of the bilayer sample for the two phase states of GST by comparing it with the blackbody under 300K, as shown in Figure 5(b). It can be intuitively found that for the amorphous state of GST, the infrared radiation of the bilayer sample is mainly concentrated in the band of 5-8 μm non-atmospheric window, and the intensity of infrared radiation in the wavelength range of 3-5 μm and 8-14 μm respectively decrease by 68.86% and 75.58% compared with blackbody by calculation, which can achieve infrared stealth together with radiative heat dissipation. Meanwhile, for the crystalline state of GST, the infrared radiation in the 8-14 μm atmospheric window band is sharply increased to 67.34% of the blackbody, which means that the infrared stealth function cannot be realized.
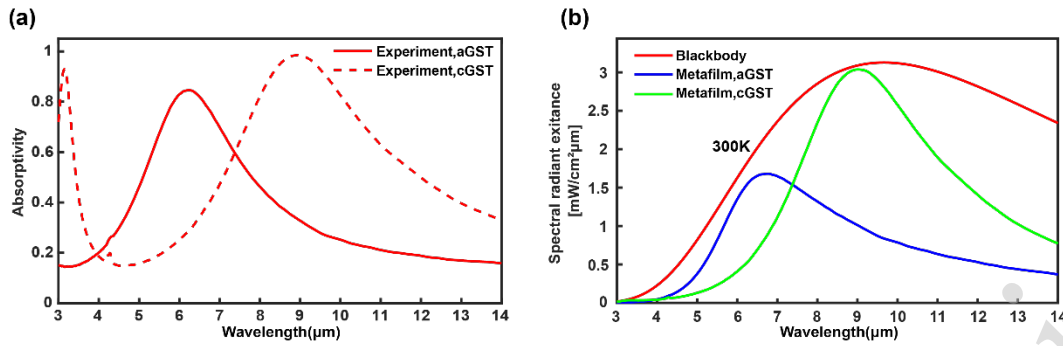
Figure 5. The infrared radiation characteristics of the sample for the two states of GST. (a) The infrared absorption spectra of the fabricated bilayer metafilm obtained by the Fourier transform infrared spectrometer (FTIR). **(b)** Spectral radiant exitance of blackbody and the fabricated bilayer metafilm at 300K when the GST is in the two states.

Finally, we demonstrate the different infrared emissivity of the samples before and after the phase transition. The temperature of the samples with both amorphous and crystalline states of GST are measured under the background temperature of 30°C, 50°C, 75°C and 100°C, respectively. Simultaneously, a silicon substrate of comparable size is placed as a reference, as shown in Figure 6. Among them, sample A is at amorphous state, sample B is the comparably sized silicon substrate reference, and the sample C is at crystalline state. We can intuitively find that compared with the sample in the crystal state, when GST is in the amorphous state, the temperature of the sample is significantly lower than the background temperature. Furthermore, as the background temperature increases, there is a continuous increase in temperature difference between samples in the two states. When the background temperature reaches 100°C, the temperature difference between the two samples is as high as 28°C, which is a very intuitive demonstration of the huge change in the infrared radiation characteristics of the sample after the phase transition. What's more, it further proves the tunable performance of our proposed switchable infrared stealth film and the possibility of practical application.

To better demonstrate the excellent properties of our proposed tunable infrared stealth metafilm, we compare it with the previous work of infrared stealth materials which are also based on the phase change material GST. The comparison is made from the aspects of constituent structure and the average emissivity in the three wavelength bands studied for the two states of GST (see Table 1). It shows the huge difference in the infrared emissivity of our proposed metafilm between the two states of GST. Furthermore, compared with the

tunable infrared stealth materials proposed by other works, the metafilm has a simpler structure with two layers, which is easier to fabricate and shows broad application prospects.
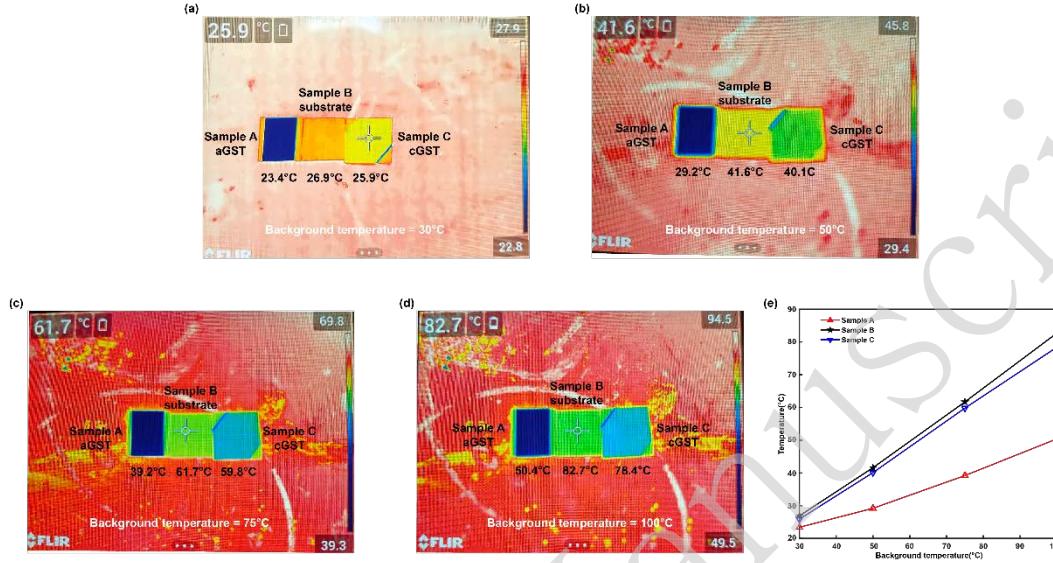

Figure 6. Demonstration of the different infrared emissivity of the samples before and after the phase transition. (**a-d**) Measured temperature of the three samples (sample A is at amorphous state, sample B is the comparably sized silicon substrate reference, and the sample C is at crystalline state) under the background temperature of 30℃, 50℃, 75℃ and 100℃. (**e**) Measured temperature curves of the three samples under the background temperature.

Table 1. Comparison between the proposed switchable infrared stealth metafilm and previously reported switchable infrared stealth materials based on the phase change material GST.

References	Constituent structure	The average emissivity when GST is in the two states							
		Amorphous state				Crystalline state			
		5-8 μm	8-14 μm	Infrared stealth	Heat dissipation	5-8 μm	8-14 μm	Infrared stealth	Heat dissipation
Zhou[60]	MIM five layers	0.21	0.04	√	×	0.79	0.15	√	√
Kang[61]	MIM three layers	0.34	0.13	√	×	0.65	0.19	√	√
Jiang[8]	MIM three layers	0.17	0.04	√	×	0.85	0.16	√	√
Qu[53]	Two layers	0.17	0.05	√	×	0.35	0.62	×	√
This paper	Two layers	0.67	0.24	√	√	0.45	0.67	×	√

Conclusions

In this paper, a non-volatile switchable infrared stealth bilayer metafilm is proposed and experimentally demonstrated based on the phase change material GST and the high

temperature resistant metal Mo. The results indicate that the infrared radiation characteristics of the metafilm will change significantly when the GST is in different states due to the great difference of the relative permittivities. Specifically, when the GST is in the amorphous state, the average emissivity of the metafilm in the 3-5 μm and 8-14 μm atmospheric window band is merely 0.31 and 0.24, respectively, enabling effective infrared stealth functionality. Additionally, in the 5-8 μm non-atmospheric window band, it exhibits an average emissivity exceeding 0.67 with a high absorptivity of 94% at 6.08 μm, indicating excellent radiative heat dissipation capabilities as well. However, when GST transitions into its crystalline state, there are substantial alterations in the infrared radiation characteristics of the structure. Particularly, there is a significant increase in average emissivity from 0.24 to 0.67 within the 8-14 μm band which tunes the metafilm to a non-stealth state. Therefore, by switching the state of GST, the target can be switched between the infrared stealth and non-stealth state, so as to achieve the purpose of dynamic control of infrared radiation. Meanwhile, the infrared radiation characteristics of the metafilm are not sensitive to incident angles and polarizations.

We investigated the infrared radiation characteristics of the bilayer sample for the two states of GST by it with the blackbody under 300K. For the amorphous state of GST, the infrared radiation of the bilayer sample is mainly concentrated in the band of 5-8 μm non-atmospheric window, while for the crystalline state of GST, the infrared radiation in the 8-14 μm atmospheric window band accounts for the majority. We demonstrate the different infrared emissivity of the samples before and after the phase transition by measuring the temperature of the samples under the background temperature of 30℃, 50℃, 75℃ and 100℃, respectively. Compared with the sample in crystalline state, it shows much lower temperature when GST is in the amorphous state. The apparent temperature of the metafilm with amorphous GST is 50.4℃ at the temperature of 100℃, and is nearly 28℃ lower than the crystalline sample under the same conditions, which fully demonstrates the great change of infrared emissivity of samples in two states.

For the annealing process in our experiment, it is realized by heating and it can only realize the amorphous-to-crystalline transition. For bi-directional switch, the crystalline-to-amorphous transition process needs a short, high-intensity power to raise the local

temperature momentarily above the melting temperature. This process can be realized by pulsed laser[62] or electric switch. In the past few years, there have been some remarkable progresses in electrical switch of chalcogenide phase change materials for tunable nanophotonic devices[63]. However, at present, almost all the research on electrical modulation is focus on small size structures, since the electrical switch of the phase change materials at a large scale is still challenging. For our research, in order to further realize the bi-directional phase transition of GST by means of electrical switch, we need to further optimize the structure and reduce the thickness of GST layer. It is also helpful to employ the high-temperature resistant metals for the design of the devices. Besides Mo, other high temperature resistant metals such as W (Tungsten) and Ti (Titanium) are also potential choices. Our work represents an important progress in exploring phase change materials for dynamic thermal radiation control and will promote the research towards practical applications of intelligent infrared stealth technology.

Materials and Methods

Sample fabrication

The silicon substrate with a $285\ nm$ oxide layer was carefully cleaned and a Mo film with the thickness of $100\ nm$ was deposited by high vacuum magnetron sputtering under room temperature and the deposition power was 100W with the speed of $0.15\ nm/s$. After that, a $360\ nm$ GST layer was deposited at the deposition power of 60W with the speed of $0.31\ nm/s$. The chamber was ceaselessly pumped to the starting pressure of $4 \times 10^{-4}\ Pa$ and the working pressure was maintained at $0.5\ Pa$ by filling the argon gas. The samples were placed on a heating stage at 200℃ (slightly above the crystallization temperature) for 10 minutes to transform into the crystal stage.

Sample measurement

The relative dielectric permittivity of the two materials were measured by an infrared ellipsometer. The infrared absorption spectra of the sample were measured by a Fourier transform infrared spectrometer (FTIR). The cross-section of the sample was observed by Scanning Electron Microscopy (SEM). The temperature of the sample was measured by a handheld infrared thermal imager (FLIR E95).

Numerical simulation

We performed the numerical simulations by using the commercial solver of COMSOL Multiphysics. We took the cross section in $x - z$ direction in the simulation and set periodic boundary conditions on each side together with the port conditions on the upper and lower boundaries. The light source was a normal incident light at TM mode (magnetic field vector is perpendicular to the incident plane). The relative permittivity of GST and Mo in infrared band were measured using a spectroscopic ellipsometer.

Acknowledgements

Author Contributions

J.-F.Z. and Z. -H. Z supervised the whole project. J.-F.Z. and C.Q. conceived the experiments. C.Q. carried out the experiments. All authors participated in the analysis of data and contributed to the writing of manuscript.

Conflict of interest

The authors declare no competing interests.

Supplementary information

Supplementary materials are available at the online version.

References

1. Graydon, O. Adaptive infrared camouflage. *Nature Photonics* **12**, 445-445 (2018).

2. Chandra, S. et al. Adaptive multispectral infrared camouflage. *ACS Photonics* **5**, 4513-4519 (2018).

3. Zhu, H. Z. et al. Multispectral camouflage for infrared, visible, lasers and microwave with radiative cooling. *Nature Communications* **12**, 1805 (2021).

4. Zhu, H. Z. et al. High-temperature infrared camouflage with efficient thermal management. *Light: Science & Applications* **9**, 60 (2020).

5. Xi, W. et al. Ultrahigh-efficient material informatics inverse design of thermal metamaterials for visible-infrared-compatible camouflage. *Nature Communications* **14**, 4694 (2023).

6. Li, M. Y. et al. Manipulating metals for adaptive thermal camouflage. *Science Advances* **6**, eaba3494 (2020).

7. Salihoglu, Q. et al. Graphene-based adaptive thermal camouflage. *Nano Letters* **18**, 4541-4548 (2018).

8. Jiang, X. P. et al. Tunable mid-infrared selective emitter based on inverse design metasurface for infrared stealth with thermal management. *Optics Express* **30**, 18250-18263 (2022).

9. Wu, Y. J. et al. Optically transparent infrared selective emitter for visible-infrared compatible camouflage. *Optics Express* **30**, 17259-17269 (2022).

10. Zhou, Z. Y. & Huang, J. Joint improvements of radar/infrared stealth for exhaust system of unmanned aircraft based on sorting factor Pareto solution. *Scientific Reports* **11**, 8251 (2021).

11. Quan, C. et al. High-temperature resistant broadband infrared stealth metamaterial absorber. *Optics & Laser Technology* **156**, 108579 (2022).

12. Zou, J. L. et al. Multiband metamaterial selective absorber for infrared stealth. *Applied Optics* **59**, 8768-8772 (2020).

13. Zhou, Y. et al. Ultra-broadband metamaterial absorbers from long to very long infrared regime. *Light: Science & Applications* **10**, 138 (2021).

14. Zhao, L. et al. All-metal frequency-selective absorber/emitter for laser stealth and infrared stealth. *Applied Optics* **57**, 1757-1764 (2018).

15. Zhang, D. et al. Ultra-wideband flexible radar-infrared bi-stealth absorber based on a patterned graphene. *Optics Express* **31**, 1969-1981 (2023).

16. Zhang, C. L. et al. Dual-band wide-angle metamaterial perfect absorber based on the combination of localized surface plasmon resonance and Helmholtz resonance. *Scientific Reports* **7**, 5652 (2017).

17. Gu, S. et al. Laser-compatible infrared stealth metamaterial based on high-temperature resistant metal. *Infrared Physics & Technology* **136**, 105072 (2024).

18. Peng, L. et al. A multilayer film based selective thermal emitter for infrared

stealth technology. *Advanced Optical Materials* **6**, 1801006 (2018).

19. Ren, Y. et al. Thermally switching between perfect absorber and asymmetric transmission in vanadium dioxide-assisted metamaterials. *Optics Express* **29**, 7666-7679 (2021).

20. Lin, K. T. et al. Structured graphene metamaterial selective absorbers for high efficiency and omnidirectional solar thermal energy conversion. *Nature Communications* **11**, 1389 (2020).

21. Li, Z. G. et al. Wavelength-selective mid-infrared metamaterial absorbers with multiple tungsten cross resonators. *Optics Express* **26**, 5616-5631 (2018).

22. Qin, B. et al. Whole-infrared-band camouflage with dual-band radiative heat dissipation. *Light: Science & Applications* **12**, 246 (2023).

23. Zhang, J. H. et al. Thin-film perfect infrared absorbers over single- and dual-band atmospheric windows. *Optics Letters* **45**, 2800-2803 (2020).

24. Kang, J. F. et al. Multifunctional-hierarchical flexibility metasurfaces for multispectral compatible camouflage of microwave, infrared and visible. *Optics Express* **31**, 29280-29299 (2023).

25. Lin, H. et al. Dual-polarized bidirectional three-dimensional metamaterial absorber with transmission windows. *Optics Express* **29**, 40770-40780 (2021).

26. Melinger, J. S. et al. THz detection of small molecule vapors in the atmospheric transmission windows. *Optics Express* **20**, 6788-6807 (2012).

27. Cheng, Y. Z. et al. Dual and broadband terahertz metamaterial absorber based on a compact resonator structure. *Optical Materials Express* **8**, 3104-3114 (2018).

28. Gao, Z. Q. et al. Ultra-wideband flexible transparent metamaterial with wide-angle microwave absorption and low infrared emissivity. *Optics Express* **29**, 22108-22116 (2021).

29. Wang, L. et al. Combined multi-band infrared camouflage and thermal management via a simple multilayer structure design. *Optics Letters* **46**, 5224-5227 (2021).

30. Chen, H. T. et al. Active terahertz metamaterial devices. *Nature* **444**, 597-600 (2006).

31. Kong, A. R. et al. Ultra-broadband all-dielectric metamaterial thermal emitter for passive radiative cooling. *Optics Express* **27**, 30102-30115 (2019).

32. Lee, S. H. et al. Switching terahertz waves with gate-controlled active graphene metamaterials. *Nature Materials* **11**, 936-941 (2012).

33. Lin, H. et al. A 90-nm-thick graphene metamaterial for strong and extremely broadband absorption of unpolarized light. *Nature Photonics* **13**, 270-276 (2019).

34. Luk'yanchuk, B. et al. The Fano resonance in plasmonic nanostructures and metamaterials. *Nature Materials* **9**, 707-715 (2010).

35. Molesky, S., Dewalt, C. J. & Jacob, Z. High temperature epsilon-near-zero and epsilon-near-pole metamaterial emitters for thermophotovoltaics. *Optics Express* **21**, A96-A110 (2013).

36. Ou, J. Y. et al. Reconfigurable photonic metamaterials. *Nano Letters* **11**, 2142-2144 (2011).

37. Ou, J. Y. et al. An electromechanically reconfigurable plasmonic metamaterial operating in the near-infrared. *Nature Nanotechnology* **8**, 252-255 (2013).

38. Papadakis, G. T. et al. Optical magnetism in planar metamaterial heterostructures. *Nature Communications* **9**, 296 (2018).

39. Qin, Z. et al. Multi-mode plasmonic resonance broadband LWIR metamaterial absorber based on lossy metal ring. *Optics Express* **30**, 473-483 (2022).

40. Schurig, D. et al. Metamaterial electromagnetic cloak at microwave frequencies. *Science* **314**, 977-980 (2006).

41. Wang, B. X. et al. Realization of a multi-band terahertz metamaterial absorber using two identical split rings having opposite opening directions connected by a rectangular patch. *Nanoscale Advances* **4**, 1359-1367 (2022).

42. Wolf, O. et al. Phased-array sources based on nonlinear metamaterial nanocavities. *Nature Communications* **6**, 7667 (2015).

43. Yang, W. H. et al. Observation of optical gyromagnetic properties in a magneto-plasmonic metamaterial. *Nature Communications* **13**, 1719 (2022).

44. Yang, Z. Y. et al. Narrowband wavelength selective thermal emitters by

confined Tamm Plasmon Polaritons. *ACS Photonics*, **4**, 2212-2219 (2017).

45. Zheludev, N. I. & Kivshar, Y. S. From metamaterials to metadevices. *Nature Materials* **11**, 917-924 (2012).

46. Zhu, W. M. et al. Microelectromechanical Maltese-cross metamaterial with tunable terahertz anisotropy. *Nature Communications* **3**, 1274 (2012).

47. Snyder, W. C., Wan, Z. M. & Li, X. W. Thermodynamic constraints on reflectance reciprocity and Kirchhoff's law. *Applied Optics* **37**, 3464-3470 (1998).

48. Sun, R. Z. et al. Broadband switching of mid-infrared atmospheric windows by VO_2 -based thermal emitter. *Optics Express* **27**, 11537-11546 (2019).

49. Lepeshov, S. & Krasnok, A. Tunable phase-change metasurfaces. *Nature Nanotechnology* **16**, 615-616 (2021).

50. Wang, Y. F. et al. Electrical tuning of phase-change antennas and metasurfaces. *Nature Nanotechnology* **16**, 667-672 (2021).

51. Guo, P. F., Sarangan, A. M. & Agha, I. A review of germanium-antimony-telluride phase change materials for non-volatile memories and optical modulators. *Applied Sciences* **9**, 530 (2019).

52. Fang, Z. R. et al. Ultra-low-energy programmable non-volatile silicon photonics based on phase-change materials with graphene heaters. *Nature Nanotechnology* **17**, 842-848 (2022).

53. Qu, Y. R. et al. Thermal camouflage based on the phase-changing material GST. *Light: Science & Applications* **7**, 26 (2018).

54. Pan, M. Y. et al. Multi-band middle-infrared-compatible camouflage with thermal management via simple photonic structures. *Nano Energy* **69**, 104449 (2020).

55. Du, K. K. et al. Control over emissivity of zero-static-power thermal emitters based on phase-changing material GST. *Light: Science & Applications* **6**, e16194 (2017).

56. Quan, C. et al. Phase change metamaterial for tunable infrared stealth and camouflage. *Optics Express* **30**, 43741-43751 (2022).

57. Xu, Z. Q. et al. Nonvolatile optically reconfigurable radiative metasurface with visible tunability for anticounterfeiting. *Nano Letters* **21**, 5269-5276 (2021).

58. Xu, Z. Q. et al. Spatially resolved dynamically reconfigurable multilevel control of thermal emission. *Laser & Photonics Reviews* **14**, 1900162 (2020).

59. Guo, X. Y. & Xie, X. Z. Planck formula for black-body radiation: derivation and applications. *Highlights in Science, Engineering and Technology* **64**, 200-204 (2023).

60. Zhou, Y. X. et al. Tunable mid-infrared selective emitter with thermal management for infrared camouflage. *Plasmonics* **18**, 2465-2473 (2023).

61. Kang, Q. L. et al. Multiband tunable thermal camouflage compatible with laser camouflage based on GST plasmonic metamaterial. *Journal of Physics D: Applied Physics* **55**, 065103 (2022).

62. Gholipour, B. et al. An all-optical, non-volatile, bidirectional, phase-change meta-switch. *Advanced Materials* **25**, 3050-3054 (2013).

63. Zhang, Y. F. et al. Electrically reconfigurable non-volatile metasurface using low-loss optical phase-change material. *Nature Nanotechnology* **16**, 661-666 (2021).